JOURNAL OF SPACECRAFT AND ROCKETS
Vol. 36, No. 5, September–October 1999

Low-Speed Aerodynamics of a Planetary Entry Capsule

Frank Y. Wang,* Özgür Karatekin,† and Jean-Marc Charbonnier‡
von Kármán Institute for Fluid Dynamics, B-1640 Rhode Saint Genèse, Belgium

Results of an investigation of the global aerodynamic coefficients and flow characterization around an Apollo-style capsule model at low speed are presented. Flow features were ascertained quantitatively with laser Doppler velocimetry, digital particle image velocimetry, and hot-wire measurements, as well as qualitatively by flow visualizations. The study revealed a meandering vortex ring around the capsule, well-organized streamwise vortices whose maximum vorticity increased in the recirculating wake before decaying farther downstream, as well as a complex array of flow separation and reattachment features. A number of particularities in the flowfield have been identified as potential candidates for triggering the onset of vehicle instability. Based on these findings, a modeling approach is proposed.

Nomenclature

Cd	= drag coefficient
Cl	= lift coefficient
Cm_{cg}	= static moment coefficient about center of gravity
D	= capsule maximum heat-shield diameter, m
f	= oscillation frequency, Hz
I	= mass moment of inertia, kg-m^2
q_∞	= freestream dynamic pressure, N/m^2
R	= local radius, m
S	= projected heat-shield area, m^2
Sr	= Strouhal number of the wake
t	= time, s
U_∞	= freestream velocity, m/s
$\underline{u}, \underline{v}, \underline{w}$	= velocity components in Cartesian coordinates, m/s
$\underline{u'^2}, \underline{v'^2}, \overline{w'^2}$	= turbulent normal stresses, (m/s)^2
$\underline{u'v'}, \overline{u'w'}$	= turbulent shear stresses, (m/s)^2
W	= amplitude of the unsteady pitching moment relative to its mean
X, Y, Z	= Cartesian coordinates
α	= angle of attack, deg
$\partial Cm_{cg}/\partial\alpha$	= static pitching moment coefficient slope, 1/rad
ρ_∞	= freestream density, kg/m^3
ω	= angular frequency of wake oscillation, rad/s

Introduction

THIS investigation is motivated by current international interest in planetary entry capsules, for example, the atmospheric reentry demonstrator (ARD) program[1] of ESA. The ARD capsule, which was onboard the Ariane 503 flight, permitted ESA to gain invaluable operational experience in launching and retrieving a crewed-type spacecraft, as well as a collection of flight data during various phases of reentry. One of the prime objectives of the ARD program is to compare the results from ground test simulation, computer predictions, and actual flight data to validate the methodology of extrapolation to flight. Research activities of this nature are very important for ensuring the proper design and safe operation of current and future planetary entry missions. For example, experience gained from ARD activities would lead to greater confidence in Europe's capability to develop manned space transportation systems such as the Crew Transport Vehicle and Crew Return Vehicle that have been proposed as part of ESA's contribution to the International Space Station. To take advantage of existing data circulating in the public domain, the ARD was modeled after the Apollo capsule.

As a side contribution to the ARD activity, the present authors have embarked on investigation of the flowfield around the ARD/Apollo capsule as the necessary first step toward understanding capsule aerodynamics, stability, parachute–wake interactions, and other associated fluid dynamics issues related to the subsonic/transonic phase of the entry.[2–4] Moreover, subsonic aerodynamics of capsules has received a resurgence of interest due to the requirement of maintaining subsonic stability in many of the upcoming planetary sampling missions,[5–10] sometimes without the benefit of parachutes.[5] To the best of the authors' knowledge, this undertaking represents one of the few detailed flow surveys of a representative capsule, and the present paper highlights the results[11,12] to date.

Experimental Approach and Setup

Examination of Apollo test data in the subsonic/transonic range[13,14] revealed that the force and moment trends are alike over the surveyed Mach number range of 0.2–1.35, suggesting that aspects of the flow around the capsule could bear similarities throughout the quoted Mach number range. This observation triggered a parallel study reported in this issue by the present authors to investigate the effect of compressibility on the global flow features around and in the wake of the Apollo shape.[15] The study was conducted at four Mach numbers: from that of essentially incompressible, 0.5, 0.7, to 0.9, in a Reynolds number range of 10^4–10^5 (based on the heat-shield diameter D in Fig. 1). The results from the aforementioned study indicated that sufficient similitude existed in the flowfield to utilize low-speed tests for extracting the flow features at higher Mach numbers. Although Reynolds numbers attainable in these tests were comparatively low relative to that of 10^7 in flight, the influence of Reynolds number would be expected to be secondary as well, particularly in practical situations in which the heat shield is facing the freestream. In such cases, the presence of a very small radius at the heat-shield edge would essentially fix a major portion of flow separation. This parallel examination led to the notion of utilizing low-speed testing, which is less cumbersome to operate and for which more diagnostic tools are available, to delineate the most salient features of the flow during the terminal phase of a reentry capsule. The terminal aerodynamics of the capsule was therefore conducted in three incompressible flow facilities, L7, L7+, and L2A, at the von Kármán Institute for Fluid Dynamics. The various characteristics of the tunnels are described in Ref. 16. The model is of the Apollo Command Module block I configuration with no protuberances,[13] shown in Fig. 1. The 180-deg-angle-of-attack position is defined as shown in Fig. 1, with freestream direction being from left to right. Using $\alpha = 180$ deg as a reference, a rotation in the counterclockwise direction reduces the angle-of-attack value. Except for flow visualizations and moment measurements, a 30-mm capsule model was supported from the tunnel side wall with a 3-mm-diam cantilever rod

Received 10 December 1998; revision received 9 June 1999; accepted for publication 13 June 1999.

*National Science Foundation International Fellow, Aeronautics and Aerospace Department; currently NRC Research Associate, Turbomachinery and Propulsion Systems Division, NASA John H. Glenn Research Center at Lewis Field, Cleveland, OH 44135. Member AIAA.

†Ph.D. Candidate, Aeronautics and Aerospace Department. Student Member AIAA.

‡Associate Professor, Aeronautics and Aerospace Department; charbonnier@vki.ac.be.

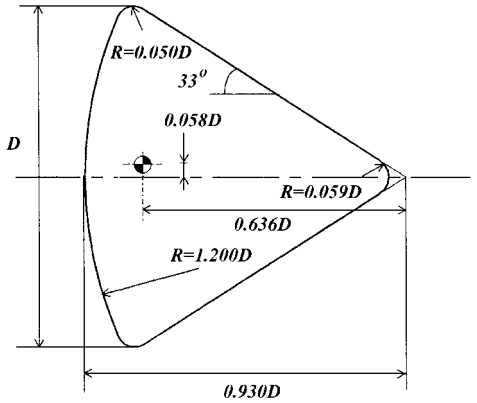

Fig. 1 Scaled drawing of the model tested.

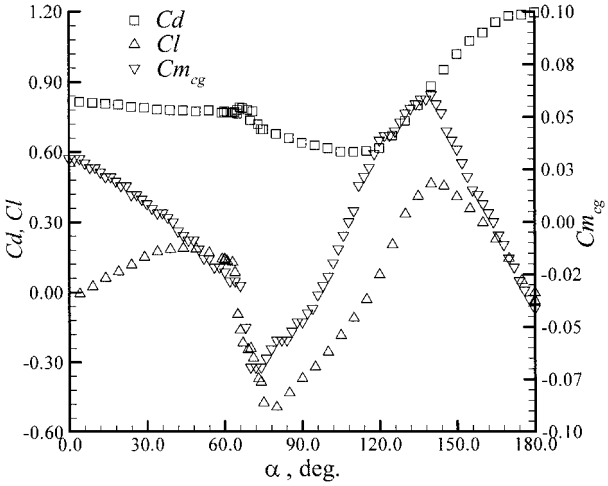

Fig. 2 Force and moment cofficients of the Apollo capsule at low speed.

affixed at the theoretical center of gravity position shown in Fig. 1. For surface oil and lightsheet visualizations, a 2-mm rod spanning the wind-tunnel test section was used to support the 30-mm capsule model. For pitching moment measurements, a 50-mm model was used in conjunction with an 8-mm transverse support through the theoretical center of gravity.[14]

Results and Discussion

Force and Moment Measurements

Lift and drag were measured with a two-component parallelogram strain-gauge balance in the L2A tunnel at a Reynolds number of 6.0×10^4 and a blockage ratio of 1.16% based on projected frontal area. The associated maximum uncertainties in lift and drag coefficients are ± 0.013 and ± 0.036, respectively. Pitching moment measurements about the theoretical center of gravity, also conducted in the L2A facility, were obtained with a torsion balance implemented in a free-to-tumble rig.[14] The moment measurements were made at a Reynolds number of 1.1×10^5 and a blockage ratio of 3.22 %. The maximum uncertainty associated with the moment coefficient is ± 0.004. The force and moment results are presented in Fig. 2. In addition to providing global aerodynamic trends, these data facilitated the selection of angle-of-attack cases for which a detailed flowfield investigation was later made. For example, pitching moment data revealed the stable trimmed positions, that is, where $Cm_{cg} = 0$ with a corresponding negative $\partial Cm_{cg}/\partial\alpha$, to be at $\alpha = 40$ and 165 deg. Because $\alpha = 165$ deg represents an orientation in which the heat shield is facing the stream, a greater emphasis has been placed on this case of practical interest during the flowfield investigation. The connections between these global aerodynamic coefficients and the flowfield investigation are presented subsequently where appropriate.

Flow Visualization

Surface oil and laser lightsheet tests were first employed for a qualitative investigation of the flowfield. These experiments were carried out in the L7 wind tunnel at a Reynolds number of 3.7×10^4 and with a blockage of 2.76%. A mixture of lamp oil, petroleum, titanium-dioxide, and oleic acid was used for the surface flow visualization. A 2-W argon-ion laser was used in conjunction with a cylindrical lens to produce a simple uncollimated lightsheet. The visualization tests were attempted for the complete range of angle of attack. However, the flowfield was successfully visualized only in the ranges of 10–110- and 150–170-deg angles of attack.

In the 10–70-deg angle-of-attack regime, that is, with the apex of the capsule facing the stream, only the leeward side of the capsule was noted to experience a broad range of change in surface oil pattern, whereas those from the heat-shield and the windward sides remained essentially unaltered. In this particular range, strong forebody vortices similar to those found on aircraft or missile nosetips began to form as the angle of attack increased from zero. These vortices were well visualized as black voids in the lightsheet and multiple separation lines in the surface oil pattern. For example, the visualization results for $\alpha = 40$ deg, one of the stable trimmed configurations, are shown in Fig. 3. Figure 3a is a lightsheet taken at the location immediately behind the model and perpendicular to the freestream in which the symmetric forebody vortex system composed of primary and secondary vortices can readily be seen. The recirculating wake, visualized in the lightsheet as a dark ring around the capsule and connecting the streamwise vortices, is also seen in

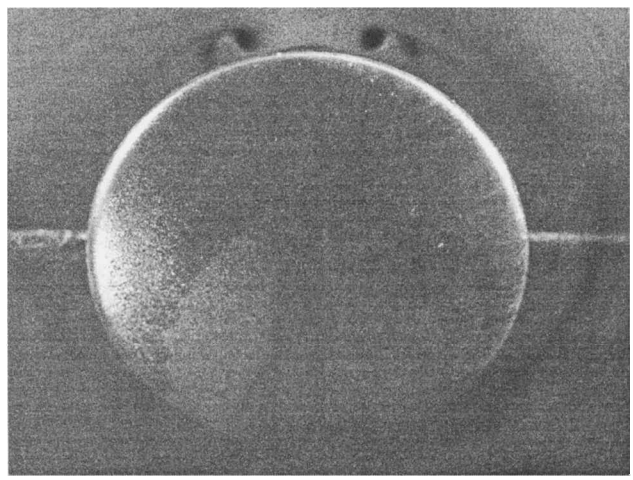

Fig. 3a Lightsheet visualization at $\alpha = 40$ deg.

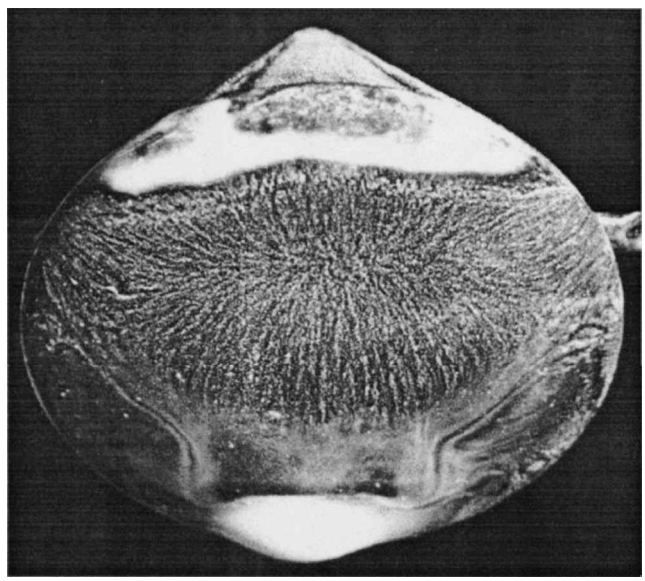

Fig. 3b Surface oil pattern on the heat shield at $\alpha = 40$ deg.

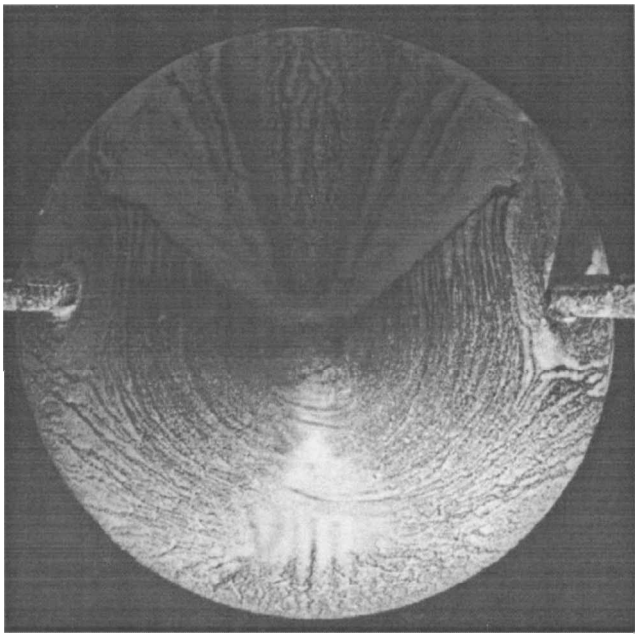

Fig. 3c Surface oil pattern on the windward side at $\alpha = 40$ deg.

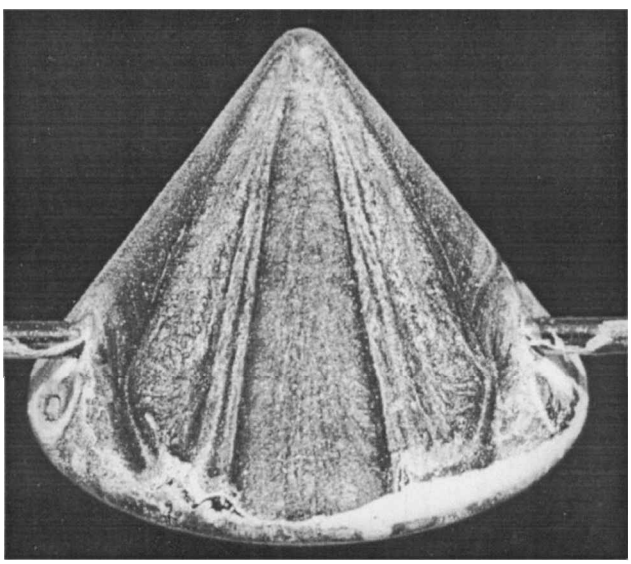

Fig. 3d Surface oil pattern on the leeward side at $\alpha = 40$ deg.

Fig. 3a. Figure 3b is the surface oil pattern on the heat shield in which the appearance of a recirculating wake is evident. The oil patterns for the windward and leeward sides are shown in Figs. 3c and 3d, respectively. Their similarity in appearance to those typically found on aircraft or missile nosetips is noted. At $\alpha = 50$ deg, the oil flow visualization showed two symmetrically positioned foci patterns appearing on the leeward side suggesting the occurrence of spiral-type separation. At the same time, the lightsheet showed the dark spots representing forebody vortices to be dramatically enlarged, resembling the appearance of vortex breakdown. At $\alpha = 60$ deg, the visualized flowfield characteristics were the same as those found at 50 deg, with the positions of the foci as revealed by oil flow visualization moving farther along toward the apex of the capsule. At $70 \leq \alpha \leq 110$ deg, streamwise vortices from the capsule were no longer evident from the lightsheet, whereas the surface oil pattern showed the formation of large recirculation bubbles over the leeward side.

The oil patterns for the $150 \leq \alpha \leq 170$ deg range possess substantial similarity and are exemplified by the case of $\alpha = 165$ deg shown in Fig. 4. These features are described as follows. At $\alpha = 150$ deg, separation lines associated with forebody vortices began to be discernible in the surface oil visualization, as typified in Fig. 4b. In addition, two large Werlé–Legendre-type separated regions were

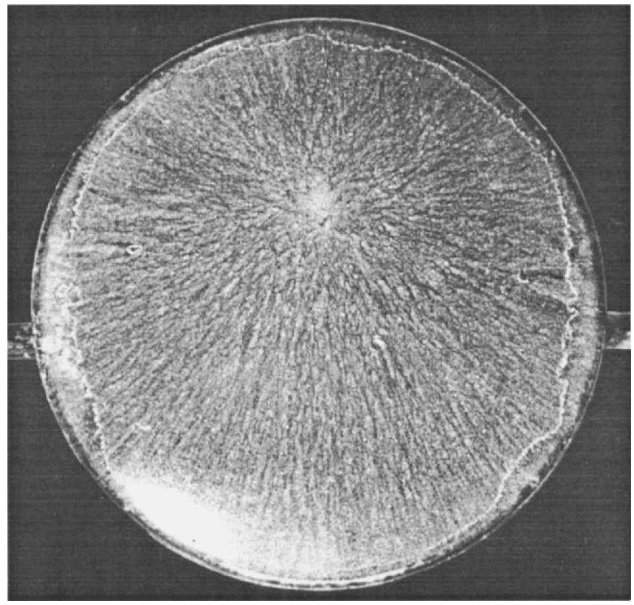

Fig. 4a Surface oil pattern on the heat shield at $\alpha = 165$ deg.

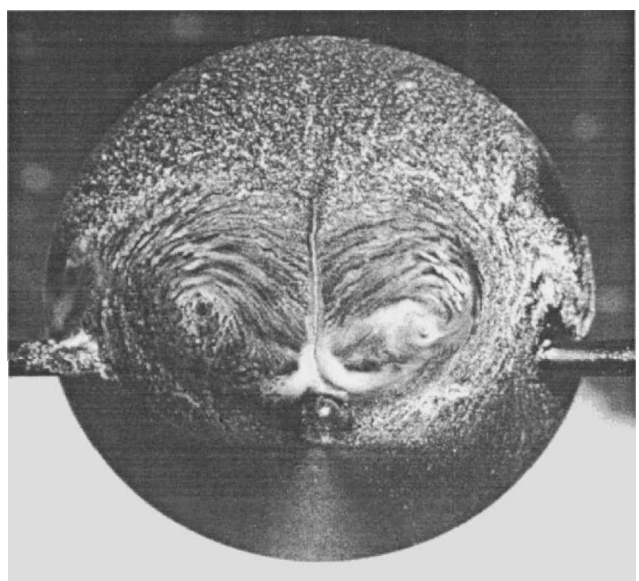

Fig. 4b Surface oil pattern on the upper side at $\alpha = 165$ deg.

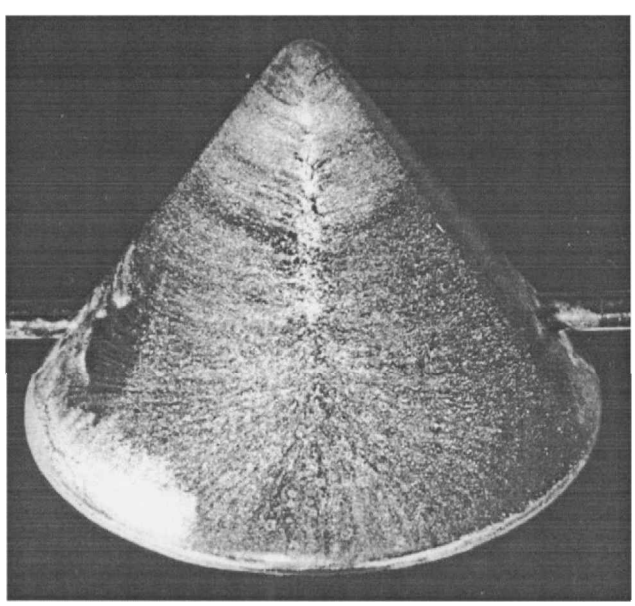

Fig. 4c Surface oil pattern on the lower side at $\alpha = 165$ deg.

found on the upper cone portion behind the heat shield. As the angle of attack increased, the area of the Werlé–Legendre separated flow progressed toward the apex. On the heat shield, a stagnation point was apparent, from which the oil streaks extended radially outward. In the lower cone portion, the appearance of a reattachment line from the apex to the heat shield was noted (Fig. 4c).

Time-Averaged Center Plane Velocity Surveys

Laser Doppler velocimetry (LDV) measurements also were performed in the L7 tunnel, at a Reynolds number of 3.7×10^4 with 2.76% blockage, and for the half of the model opposite the supporting rod. A TSI™ two-component backward scattering LDV system was used to characterize the time-averaged flowfield. The system was set to collect either 2048 samples per measurement location or as many data points as possible within a 90-s window, depending on the condition first reached. In the latter scenario, a minimum of 800 data points were collected at each measured location. Seed particles on the order of 1-μm diameter were generated by vaporizing oil droplets introduced through the blower into the tunnel diffuser. Complete three-dimensional wake flows were mapped out at three angles of attack for a distance up to two capsule diameters downstream. However, the flow diagnostics around the capsule body were restricted to u and v components. The LDV raw data were processed with a transit time weighting bias correction scheme, and the commercial software Tecplot™ was utilized for data visualization. The uncertainty in the measured velocity is 1%.

The LDV measurements were taken along the symmetry plane of the capsule at $\alpha = 90$, 100, 110, 123, 135, 147, 155, 165, 175, and 180 deg. These surveys had spatial resolutions in the Y direction of 0.5 mm near the capsule surface and, depending on the particular circumstance, 1–2 mm in regions inside and 2–3 mm outside of the recirculating wake. The spatial resolution in the X direction ranged from 2–3 and 3–10 mm inside and outside of the recirculating region, respectively. Typical results from these surveys are shown in Fig. 5 in which the streamtrace feature (computed from a predictor–corrector integration algorithm) of the data visualization software was used to delineate the recirculating wake. The more comprehensive three-dimensional survey at $\alpha = 165$ deg conclusively showed that the recirculating pattern seen in Fig. 5 is in fact a slice through a vortex ring. The flow from one side of the capsule was observed, for example, in the $\alpha = 165$ deg case, to first shed into the near wake from the upper cone part and then remarkably impinge on the lower side. The accompanied surface oil flow visualization, that is, Fig. 4c, also supports this notion inasmuch as a reattachment line is seen along the center plane in the underside of the capsule. The reattached flow then proceeded toward the cone–sphere junction, merged with the shear layer separated from the lower portion of the heat-shield edge, and subsequently streamed again into the wake.

The center plane LDV data revealed a significant bias in the spatial distribution of turbulence intensity {expressed as $\sqrt{[\frac{1}{2}(\overline{u'^2} + \overline{v'^2})]}/U_\infty$} and the normalized Reynolds stress, that is, $\overline{u'v'}/U_\infty^2$, in parts of the flow. For all angles of attack examined, the wake closure regions exhibited very large turbulence intensity and normalized Reynolds stress on the orders of at least 25% and 0.03, respectively. These high values are not unexpected inasmuch as this is the region where all of the turbulent shear layer fluids impinge on each other and then are abruptly diverted. For angle-of-attack cases that produce high lift, in addition to the vicinity of the wake closure location, these high levels of turbulence intensity and normalized Reynolds stress are also found on one side of the recirculating wake only. For example, in the case of $\alpha = 165$ deg, turbulence intensity and Reynolds stress are shown in Fig. 6 (with the lightly drawn streamtraces superimposed) in which their high contour levels in the wake closure and lower recirculating wake regions are readily noted. The same bias is found in $\alpha = 123$, 135, 147, and 155 deg, incidences corresponding the capsule experiencing high lift. The data for a representative low or nonlifting case, such as those of $\alpha = 100$ deg, are shown in Fig. 7. The turbulence intensity and Reynolds stress are distributed rather evenly on the upper and lower sides of the wake, with both quantities having their highest values around the wake closure locations.

A compilation of the stagnation locations in the wake at various angles of attack is given in Table 1. The variables X and Y are the coordinates parallel and normal to the freestream direction with respect to the capsule apex for each angle of attack. The pressure drag is the predominant drag component in a blunt body and should

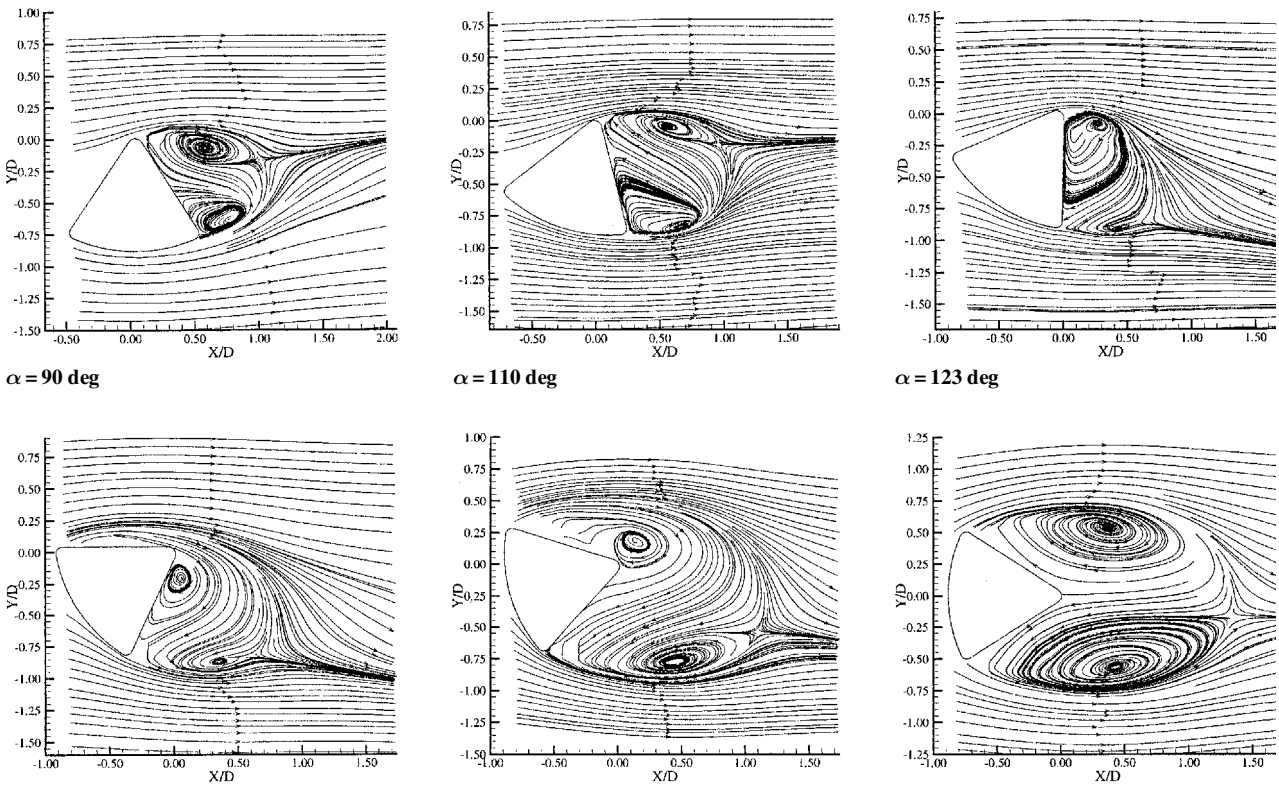

Fig. 5 Representative time-averaged, center plane velocity surveys at various angles of attack.

Table 1 Time-averaged wake stagnation point locations

α, deg	X/D	Y/D
90	+1.01	−0.15
100	+1.01	−0.16
110	+0.98	−0.19
123	+0.55	−0.88
135	+0.46	−0.87
147	+0.61	−0.82
155	+0.88	−0.76
165	+1.11	−062
175	+1.32	−0.31
180	+1.36	−0.13

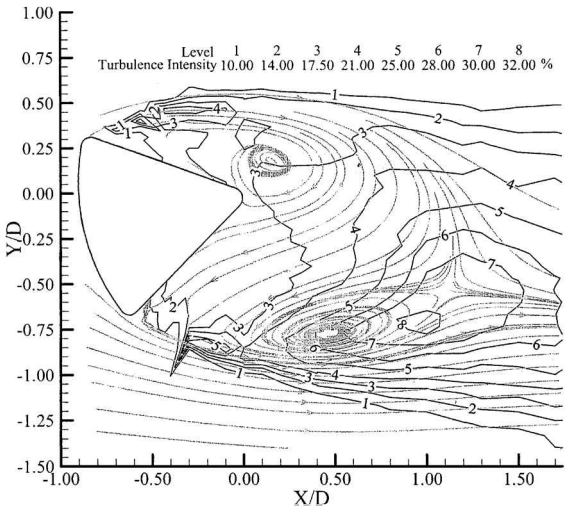

Fig. 6a Turbulence intensity for $\alpha = 165$ deg.

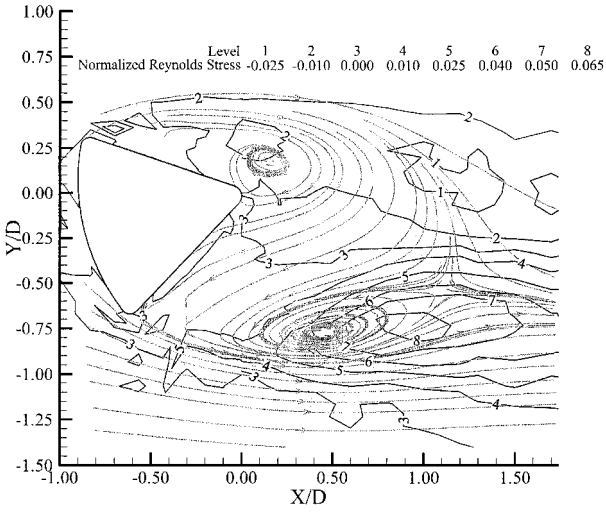

Fig. 6b Reynolds stress for $\alpha = 165$ deg.

manifest itself in the size of the wake in a manner consistent with the two-dimensional counterpart. Consequently, the dimension of the recirculating wake along the model center plane would then provide a qualitative indication of the drag. Similarly, the vertical position of the stagnation point in the wake relative to the model is indicative of the upwash or downwash that existed, thus associated with the amount of lift experienced by the body. The migration of the wake closure point vs angle of attack is well correlated with drag and lift trends shown in Fig. 2, which supports the aforementioned notion. In the $\alpha = 180$ deg case, the wake stagnation point is noted to exhibit some degree of asymmetry that could be due to reasons ranging from the $\frac{1}{2}$-deg uncertainty in setting the model angle of

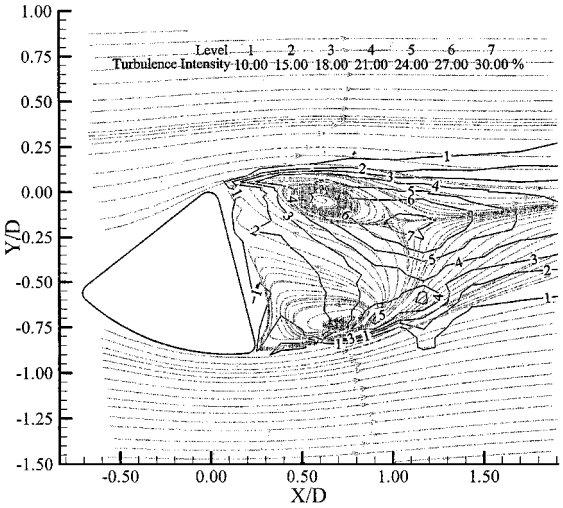

Fig. 7a Turbulence intensity for $\alpha = 100$ deg.

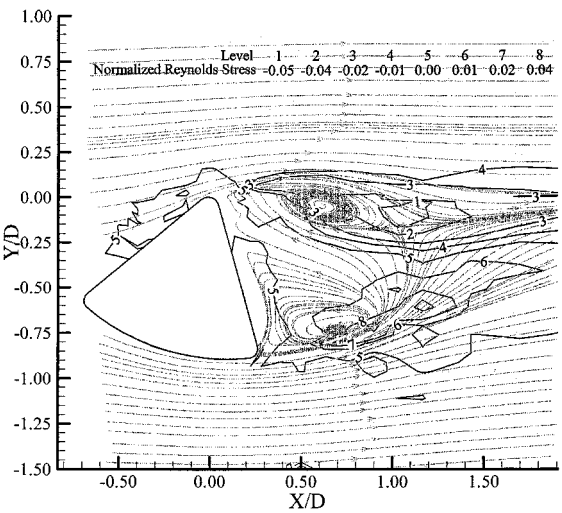

Fig. 7b Reynolds stress for $\alpha = 100$ deg.

attack, to slight model imperfection, to the incoming freestream flow being less than perfectly uniform. The exact cause of the observed asymmetry was not pursued.

Time-Averaged Crossflow Velocity Surveys

The angles of attack in the neighborhood of 165 deg also represent typical capsule orientations prior to parachute deployment. Comprehensive three-dimensional LDV measurements were consequently made for the model at $\alpha = 147$, 155, and 165 deg to ascertain the crossflow characteristics for these configurations. For the 147- and 155-deg-angle-of-attack cases, the surveys included three stations up to two capsule diameters downstream, with the middle location at the plane of wake closure. In the $\alpha = 165$ deg case, the same two capsule diameter downstream survey limit encompassed 10 crossflow measurement planes. To obtain three-dimensional data with a two-component LDV system, uv and uw measurements were made separately at a given location. A constant spatial resolution of 2 mm was employed in these measurements. Typical results from these crossflow surveys are shown in Fig. 8, where the projection of the capsule (with apex location at the origin) on the measurement plane is superimposed for reference. The turbulence intensity, computed as $\sqrt{[\frac{1}{3}(u'^2 + v'^2 + w'^2)]}/U_\infty$, is again found to have much higher levels in the lower portion of the wake. The normalized Reynolds stresses, $\overline{u'v'}/U_\infty^2$ and $\overline{u'w'}/U_\infty^2$, although both also have their respective maximum values in the lower half of the wake, did not occur in the same general area. These trends were found consistently for the three angle-of-attack cases in which crossflow surveys were made.

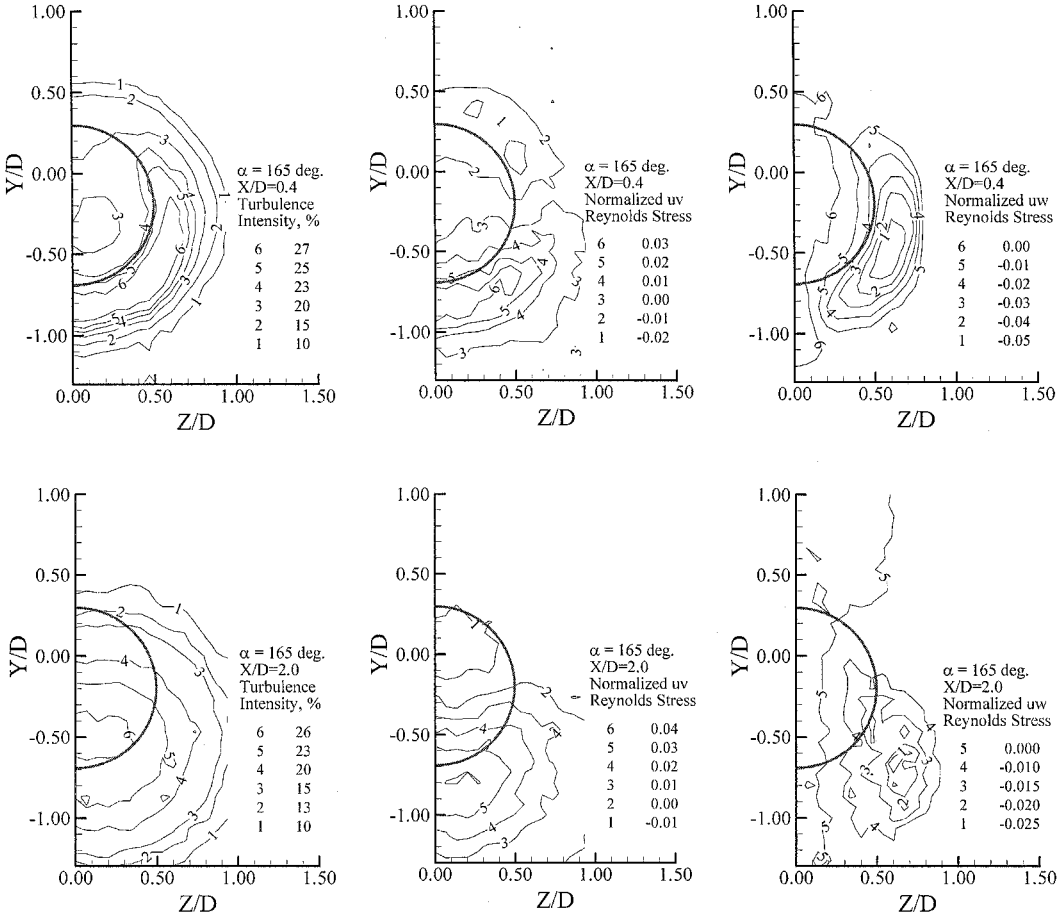

Fig. 8 Turbulent characteristics in the crossflow plane inside ($X/D = 0.4$) and outside ($X/D = 2.0$) of the recirculating wake.

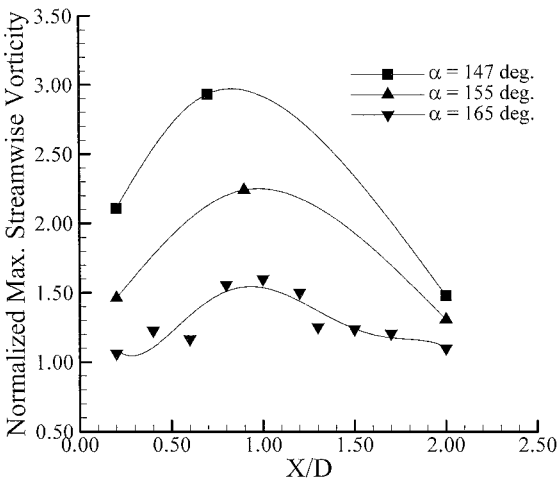

Fig. 9 Maximum streamwise vorticity characteristic.

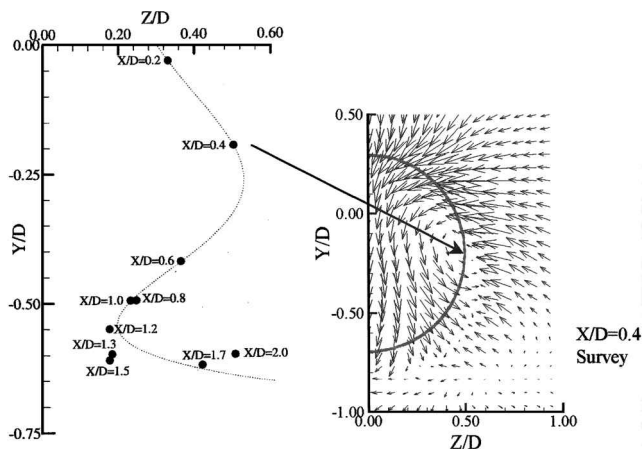

Fig. 10 Trajectory of the $\alpha = 165$ deg streamwise vortices as determined from the crossflow pattern.

The maximum vorticity within the convecting vortices, computed by central differencing crossflow velocity data and normalizing by U_∞/D, are summarized in Fig. 9. An interesting feature is the trend of increasing streamwise vorticity of the trailing vortices as they approached the rear stagnation point in the wake. For each of the three angles of attack investigated, maximum streamwise vorticity was found to increase in strength and reach the greatest value near the crossflow plane of wake closure first, before subsequently decaying, a result that would impact parachute deployment strategy. From the 165-deg crossflow surveys, the trajectory of the streamwise vortex core can also be inferred (Fig. 10). The vortex center here has been approximated as the location of zero swirl, as shown in Fig. 10. In passing through the recirculating wake, the trajectory of the streamwise vortices is apparently significantly affected by the surrounding convective flow, as well as the mutually induced velocity field. As a consequence, streamwise vortices are the closest to each other in the vicinity of wake stagnation point and subsequently diverge and descend farther.

Instantaneous Velocity Surveys

Instantaneous velocity measurements along the plane of symmetry for $\alpha = 147$, 155, and 165 deg were obtained with the digital particle image velocimetry (DPIV) technique whose setup included a BMI Nd:Yag laser (with two cavities each pausing at 10 Hz) and a TSI 640×480 pixels cross-correlation camera. These measurements were made in the L7+ tunnel at a Reynolds number of 3.1×10^4 and at 0.7% blockage. Because of the problem of intense light reflection from the model, DPIV measurements were made

behind the body only. Such a restricted data field was nonetheless large enough to have contained a sufficient portion of the vortex ring, as shown in the following $\alpha = 165$ deg results. These images were treated with a Gaussian cross-correlation algorithm with subpixel interpolation to achieve a particle displacement resolution of 0.1 pixel. An interrogation window of 48×48 and overlapping of 13×16 pixels were used in reducing the DPIV data, resulting in 35×35 vectors covering an area represented by 2.5×2.3 capsule diameters. The spatial resolution of these measurements is, thus, taken as 2.21×2.03 mm. The uncertainty in DPIV measurements is mainly from resolving the minimum particle displacement within a given interrogation area that is taken as 0.1 pixel. This resolution in pixel displacement then yields an uncertainty of 4% in freestream velocity. As imposed by the pulse frequency of the Nd:Yag laser, DPIV data were acquired at 10 Hz, that is, 10 cross-correlated images. Although this sampling rate, as concluded from hot-wire surveys to be described later, was insufficient to resolve fully the temporal evolution of the wake, very insightful information was obtained.

The DPIV data revealed a meandering vortex ring in the wake. Correspondingly, a substantial movement in the wake closure point was noted. Some instantaneous data from these tests are shown in Figs. 11a–11d, in which streamtraces were again utilized to visualize the vector fields. Note that the rear stagnation point in Fig. 11b was located at $(X/D = 0.75, Y/D = 0.11)$, representing a movement of 0.73 capsule diameters in the vertical direction from its time-averaged position. Inasmuch as the shape and the evolution of the wake would provide a heuristic indicator of the forces on the body, the observed event suggests the capsule is experiencing unsteady loading.

Another feature noted was the occurrence of multiple corotating swirling structures at the lower portion of the wake as shown in Figs. 11c and 11d. Given the spatial resolution of the vector field, small-scale vortices stemmed from separation at the cone–sphere junction would not be resolved in these DPIV images. A question that then arises would be whether these swirling features are associated with shedding of the vortex ring. The available data do not support the notion that they were, as multiple vortices such as those shown in Figs. 11c and 11d were found only at the lower half of the wake. If vortex rings were shed, it should reveal itself as two (or the multiple of) additional swirling patterns on both upper and lower parts of the wake. The additional swirl structure found is believed to be from the vortex loop developed as the consequence of the capsule experiencing unsteady lift. As the wake closure point oscillated, a corresponding change in lift was associated. A new starting vortex was subsequently deposited into the wake, analogous to the wake evolution of an impulsively driven blunt body shown in Ref. 17. Because the three angle-of-attack cases for which DPIV surveys were made, that is, $\alpha = 147$, 155, and 165 deg, were positive lifting cases, additional counterclockwise swirling patterns were found only in the lower part of the wake support for the proposed mechanism. The shedding of the starting vortices from the capsule would also be manifested as high levels of turbulence intensity and Reynolds stresses in the wake. The high values in these turbulent quantities distributed at the lower portion of the capsule as

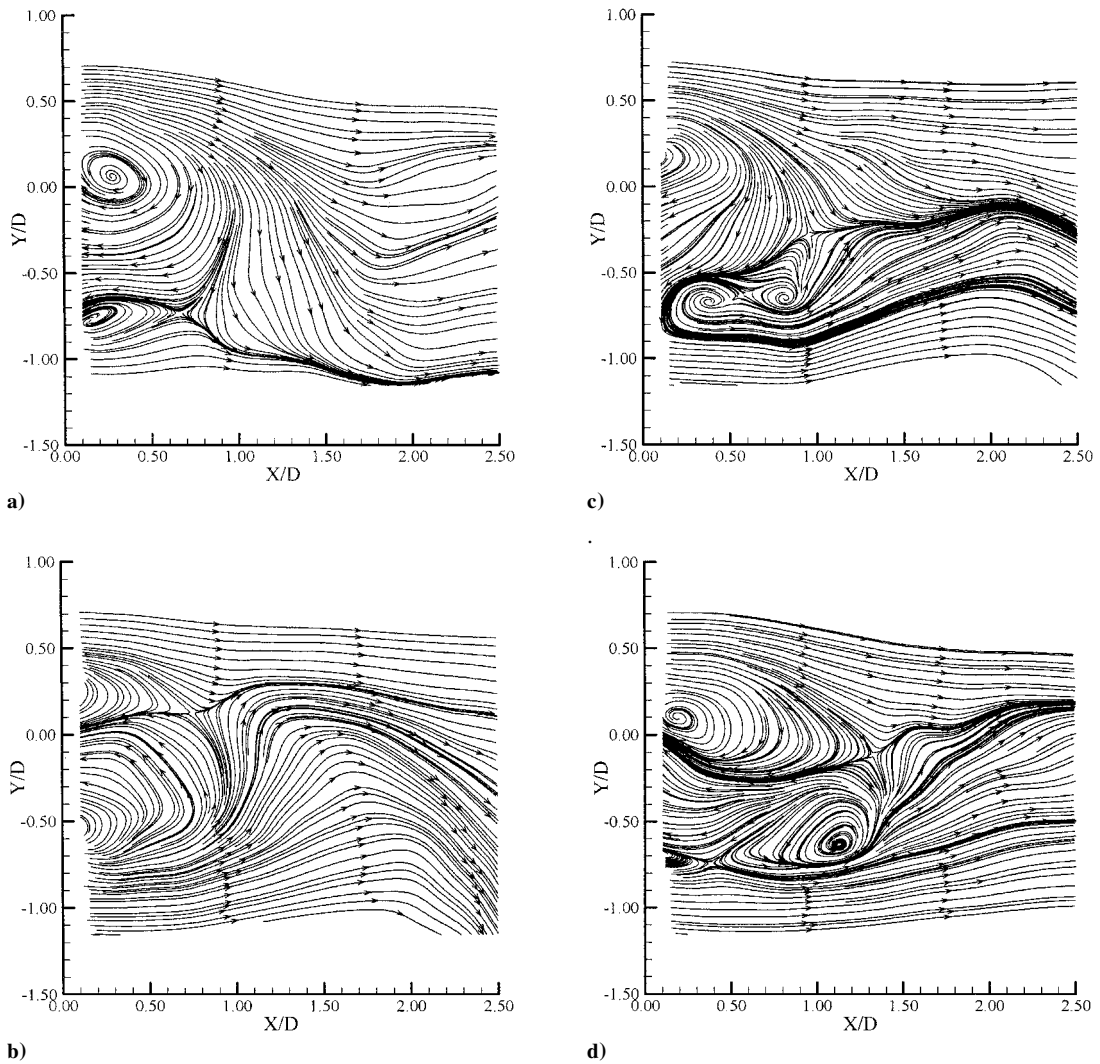

Fig. 11 Sample instantaneous DPIV images from the α = 165 deg center plane survey.

seen in LDV data were consistent with this notion and may be taken as further circumstantial evidence of the proposed flow description. In the event of vortex ring shedding from the recirculating wake, no such spatial bias in the aforementioned statistical quantities would be anticipated.

On the basis of the vortex-filament consideration, a stable recirculating wake behind a blunt body cannot exist unless it is perfectly circular.[18] Any deviation from this ideal shape would cause the various parts of the ring to experience different induced velocities thereby deforming it continuously. The vortex ring behavior is further complicated by the separated shear layer of the heat-shield edges, and the streamwise and starting vortices. These neighboring structures provide mechanisms by which the recirculating wake can change its shape via exchanging fluids with the surrounding.

Spectral Characteristics

Center plane hot-wire measurements throughout the near wake of the $\alpha = 165$ deg case were thus performed in the interest of determining whether any parts of the flowfield exhibited some degree of periodicity. A single-component, 5-μm tungsten hot-wire probe developed in-house was used. The study was carried out again in the L7 tunnel at a Reynolds number of 3.7×10^4 and a blockage of 2.76%. Acquisition of the hot-wire data was performed over 1 s and fed to a Hewlett–Packard signal analyzer. When individual frequency spectrum displays were viewed, no distinguishable peaks were observed. However, notable frequency peaks emerged when these records were averaged. During the $\alpha = 165$ deg investigation, 2000 such spectral samples were used in the averaging process at each measurement location and plotted as the power spectra density vs frequency. The investigation revealed that the vortex ring meandered at the flapping motion frequency of the recirculating wake. Although 2000 hot-wire records were used in each measurement location in the $\alpha = 165$ deg investigation, 200 samples were later revealed to be sufficient for a dominate frequency in the flow to emerge. Therefore, 200 samples were used in the subsequent investigation.

For other angles of attack, the hot-wire was placed at approximately 3 mm horizontally behind the wake closure point indicated by the mean velocity field. The probe was then traversed vertically to ensure the consistency of detected frequency. Except for the range of $\alpha = 60$–120 deg, a very distinct dominant frequency is found for each angle of attack examined. Within the $\alpha = 60$–120 deg range, the amplitude of the frequency peak is reduced compared to background turbulence, and its variance is increased. Nevertheless, a characteristic frequency is still identifiable. Examples of the spectrum characteristics are shown in Fig. 12. The data were reduced to Strouhal number (with a maximum uncertainty of ± 0.01), and their variation with angle of attack is shown in Fig. 13.

Because the probe was located in close proximity to the steady-state wake closure point, the measured frequency represents twice that of the wake flapping motion. The comprehensive hot-wire surveys in the 165-deg-angle-of-attack case, which included measurements in the underside of the capsule, showed that reattachment of the wake flow occurs semiperiodically at the same frequency as the wake oscillation. The dynamics of the reattached wake flow, therefore, induces an external moment and may be modeled by the method of Ref. 19, which is a combined computational–experimental study of flow past a freely rotatable square cylinder. In Ref. 19, the wake is considered as an external forcing moment and the quasi-steady approach exhibited good qualitative agreement with the experiments. In the case of negligible aerodynamic damping, which typically is

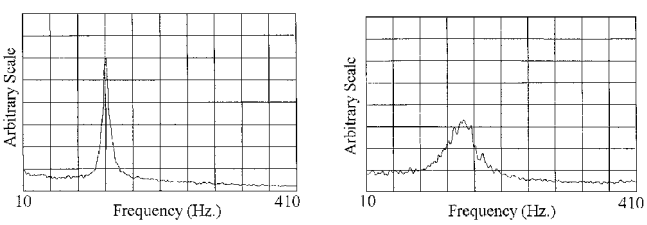

$\alpha = 30$ deg $\alpha = 80$ deg

Fig. 12 Examples of averaged spectral signals.

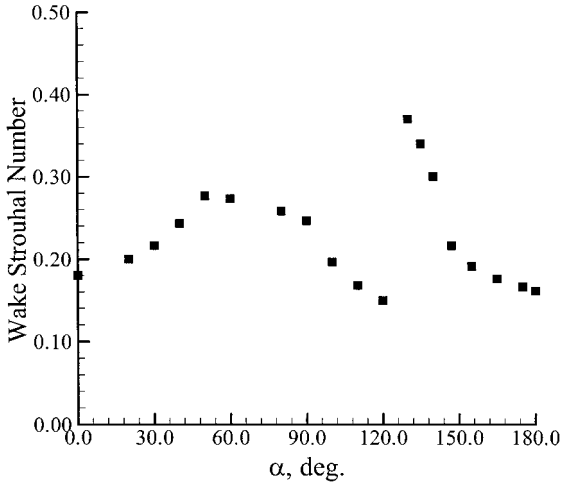

Fig. 13 Strouhal number variation.

an appropriate assumption for capsules around trimmed positions, the rotational response of the capsule is then given by

$$I\frac{\mathrm{d}^2\alpha}{\mathrm{d}t^2} + q_\infty SD\frac{\partial Cm_{\mathrm{cg}}}{\partial\alpha}\alpha = q_\infty SD \cdot W \cdot Cm_{\mathrm{cg}} \cdot \cos(\omega t) \qquad (1)$$

The inability to experimentally quantify W is for the time being circumvented by using the computational result of Ref. 19 at the same Reynolds number range. As the low-speed pitching moment and wake Strouhal number values are representative of the entire subsonic regime,[15] they have been taken from the incompressible data presented herein. Such an exploratory calculation indicates that, at a typical parachute deployment condition of 14.7-km altitude and Mach number of 0.75, a limit cycle of 2-deg oscillation would start to set in for an Apollo command module boilerplate configuration[20] having the center of gravity location shown in Fig 1. The amplitude of the oscillation will grow directly with the increasing density associated with flight descent. At the same time, the ratio of the capsule natural frequency to wake excitation frequency, expressed as

$$\frac{f_{\mathrm{capsule}}}{f_{\mathrm{wake\ excitation}}} = \sqrt{\frac{|(\partial Cm_{\mathrm{cg}}/\partial\alpha)|\rho_\infty D^5}{8\pi I Sr^2}} \qquad (2)$$

reaches 0.28. The two frequencies are, thus, within the same order of magnitude of each other. It remains a subject of further study to determine the critical ratio for which a synchronization,[21] otherwise known as lock-in type of phenomenon, would occur, which could then set the body into autorotation.

Conclusion

The study of the incompressible flowfield around an Apollo capsule model has been presented. Based on a statistically meaningful sample size, the time-averaged flowfield is found to be characterized by a vortex ring around the capsule and the presence of streamwise vortices. Unsteady measurements delineated instantaneous structures of the wake flow and revealed the existence of a well-defined Strouhal number.

The shedding of vortex ring, as commonly observed in blunt-body wakes at lower Reynolds number, did not appear to have occurred, judging from the present information. Instead, the data are more inclined to suggest the continuous presence of an unsteady vortex ring around the capsule and the shedding of starting vortices as the body experiences unsteady lift. It is conjectured that the Strouhal number found is associated with the meandering of the vortex ring around the capsule, as well as flow reattachment of the body. Inasmuch as the stability of the wake is inevitably linked to the forces on the body, unsteadiness in any of the aforementioned flow structures could provide a source of unfavorable excitation to the capsule and could cause the onset of instability. The reattached wake flow as illustrated in the $\alpha = 165$ deg case could also conceivably interfere with the separation process at the sphere–cone junction, thereby affecting the

loading on the vehicle. Additional experiments, along with unsteady numerical computations, are underway to further quantify the flowfield impact on the various aerodynamic coefficients. The results of the current endeavor complemented the existing global subsonic aerodynamic quantities of the Apollo capsule.[11,14,15] Moreover, the detailed flow documentation provided a valuable database for validating and guiding the simultaneous numerical simulation effort being carried out on the same geometry elsewhere. Such a database is of interest not only in the context of the ARD program, but for other planetary entry missions that demand accurate predictions of certain low subsonic flight qualities, as well as the near-wake characterization of a generic sphere–cone blunt lifting body.

Acknowledgments

The partial financial support from the ESA's General Support Technical Programme, Micro-Aerodynamics of Complex External and Internal Configurations, is acknowledged with appreciation. The financial support from the National Science Foundation International Fellowship Program Grant INT-9600318 for the first author and the Scientific and Technical Research Council of Turkey for the second author are likewise gratefully acknowledged. Special thanks also go to the von Kármán Institute for Fluid Dynamics support staff, as well as short-training program participants N. Claessens (of the Royal Military Academy Belgium), L. Fava, L. Tomasini, and J. Walden, for their assistance.

References

[1]"Ariane 503/ARD: A Successful Complete European Space Mission," ESA, Press Release 46-98, Oct. 1998.

[2]Baillion, M., "Blunt Bodies Dynamic Derivatives," *Capsule Aerothermodynamics*, AGARD Rept. 808, May 1997, pp. 8.1–8.28.

[3]Canning, T. N., and Edwards, T. M., "Galileo Probe Parachute Test Program: Wake Properties of the Galileo Probe at Mach Numbers from 0.25 to 0.95," NASA RP-1130, April 1988.

[4]Ericsson, L. E., and Reding, J. P., "Re-Entry Capsule Dynamics," *Journal of Spacecraft and Rockets*, Vol. 8, No. 6, 1971, pp. 579–586.

[5]Mitcheltree, R. A., and Kellas, S., "A Passive Earth-Entry Capsule for Mars Sample Return," International Symposium Atmospheric Reentry Vehicles and Systems, Arcachon, France, March 1999.

[6]Mitcheltree, R. A., Fremaux, C. M., and Yates, L. A., "Subsonic Static and Dynamic Aerodynamics of Blunt Entry Vehicles," AIAA Paper 99-1020, Jan. 1999.

[7]Mitcheltree, R. A., and Fremaux, C. M., "Subsonic Dynamics of Stardust Sample Return Capsule," NASA TM 110329, March 1997.

[8]Chapman, G. T., and Yates, L. A., "Dynamics of Planetary Probes—Design and Testing Issues," AIAA Paper 98-0797, Jan. 1998.

[9]Taverna, M. A., "Microsats to Back Up Sample Return Missions," *Aviation Week and Space Technology*, 15 Feb. 1999, pp. 22, 23.

[10]Taverna, M. A., "Mercury and Venus Sample Returns Eyed," *Aviation Week and Space Technology*, 15 Feb. 1999, pp. 23, 24.

[11]Wang, F. Y., Karatekin, Ö., and Charbonnier, J.-M., "An Experimental Study of the Flow-Field Around an Apollo Capsule at Low Speed," AIAA Paper 98-0319, Jan. 1998.

[12]Karatekin, Ö., Wang, F. Y., and Charbonnier, J.-M., "Near-Wake of a Three-Dimensional Bluff Body at Angles of Attack," American Society of Mechanical Engineers, Fluids Engineering Div. Summer Meeting, FEDSM98-5185, Washington, DC, June 1998.

[13]Moseley, W. C., Moore, R. H., and Hughes, J. E., "Stability Characteristics of the Apollo Command Module," NASA TND-3890, March 1967.

[14]Strutzenberg, R., "Stability of a Planetary Entry Vehicle," von Kármán Inst. for Fluid Dynamics, Project Rept. 1995-08, Rhode Saint Genèse, Belgium, June 1995.

[15]Wang, F. Y., Charbonnier, J.-M., Karatekin, Ö., and Paris, S., "Utilization of Low-Speed Experiments in Transonic Capsule Stability Research," *Journal of Spacecraft and Rockets*, Vol. 36, No. 5, 1999, pp. 774–776.

[16]"von Kármán Institute for Fluid Dynamics—Facilities and Instrumentation," von Kármán Inst. for Fluid Dynamics, Rhode Saint Genèse, Belgium, 1991.

[17]Brücker, C., "3-D Scanning-Particle-Imaging-Velocimetry: Technique and Application to a Spherical Cap Wake Flow," *Applied Scientific Research*, Vol. 56, No. 2/3, 1996, pp. 157–179.

[18]Landahl, M. T., "Numerical Modeling of Blunt-Body Flows—Problems and Prospects," *Proceedings of the Symposium on Aerodynamic Drag Mechanisms of Bluff Bodies and Road Vehicles*, edited by G. Sovran, T. Mortel, and W. T. Mason, Plenum, New York, 1978, pp. 289–311.

[19]Zaki, T. G., Sen, M., and Gad-el-Hak, M., "Numerical and Experimental Investigation of Flow Past a Freely Rotatable Square Cylinder," *Journal of Fluids and Structures*, Vol. 8, No. 6, 1994, pp. 555–582.

[20]"Weight, Balance and Inertia for the Apollo Boilerplate Configurations," North American Aviation, Inc., NASA-CR-117235/SID-62-1434, June 1963.

[21]Sarpkaya, T., "Vortex-Induced Vibrations—A Selective Review," *Journal of Applied Mechanics*, Vol. 46, June 1979, pp. 241–258.

J. R. Maus
Associate Editor